2020

IMPACT RESPONSE OF FLUID-SATURATED GRANULAR BEDS AND DENSE SUSPENSIONS

Causley, Neil A.

Monterey, CA; Naval Postgraduate School

NAVAL POSTGRADUATE SCHOOL

MONTEREY, CALIFORNIA

THESIS

IMPACT RESPONSE OF FLUID-SATURATED GRANULAR BEDS AND DENSE SUSPENSIONS

by

Neil A. Causley

June 2020

Thesis Advisor:	Abram H. Clark IV
Second Reader:	Emil P. Kartalov

THIS PAGE INTENTIONALLY LEFT BLANK

REPORT DOCUMENTATION PAGE	*Form Approved OMB No. 0704-0188*

1. AGENCY USE ONLY *(Leave blank)*	**2. REPORT DATE** June 2020	**3. REPORT TYPE AND DATES COVERED** Master's thesis

4. TITLE AND SUBTITLE IMPACT RESPONSE OF FLUID-SATURATED GRANULAR BEDS AND DENSE SUSPENSIONS	**5. FUNDING NUMBERS**
6. AUTHOR(S) Neil A. Causley	
7. PERFORMING ORGANIZATION NAME(S) AND ADDRESS(ES) Naval Postgraduate School Monterey, CA 93943-5000	**8. PERFORMING ORGANIZATION REPORT NUMBER**
9. SPONSORING / MONITORING AGENCY NAME(S) AND ADDRESS(ES) N/A	**10. SPONSORING / MONITORING AGENCY REPORT NUMBER**

11. SUPPLEMENTARY NOTES The views expressed in this thesis are those of the author and do not reflect the official policy or position of the Department of Defense or the U.S. Government.

12a. DISTRIBUTION / AVAILABILITY STATEMENT Approved for public release. Distribution is unlimited.	**12b. DISTRIBUTION CODE** A

13. ABSTRACT (maximum 200 words)

Systems of sub-millimeter solid particles immersed in a simple fluid can exhibit a dramatic increase in flow resistance when they are rapidly sheared, often called discontinuous shear thickening (DST). A related process is impact-induced solidification, which occurs when an intruder is driven into a particle-fluid mixture. The resultant hardening is sufficient to dampen the movement of the intruder to essentially stop it in a distance much shorter than it would in other fluids. However, the fundamental physical processes that give rise to these behaviors are not well understood. An improved description would have several military applications, such as under-vehicle armor and pipe jacketing. It also could provide a better understanding of how mines interact with wet soils. This thesis presents a fundamental experimental and theoretical study of low-speed impacts into systems of glass beads of varying sizes mixed with water. Our results show that current models fail to capture many aspects of the behavior (e.g., how the peak stresses during impact depend on the initial impact speed and the particle diameter), suggesting that new theoretical descriptions are needed.

14. SUBJECT TERMS refractive index matching, dense suspension, saturated granular bed, added mass, Darcy flow, Reynolds dilatancy, discontinuous shear thickening, DST	**15. NUMBER OF PAGES** 61
	16. PRICE CODE

17. SECURITY CLASSIFICATION OF REPORT	**18. SECURITY CLASSIFICATION OF THIS PAGE**	**19. SECURITY CLASSIFICATION OF ABSTRACT**	**20. LIMITATION OF ABSTRACT**
Unclassified	Unclassified	Unclassified	UU

NSN 7540-01-280-5500 Standard Form 298 (Rev. 2-89) Prescribed by ANSI Std. 239-18

THIS PAGE INTENTIONALLY LEFT BLANK

Approved for public release. Distribution is unlimited.

IMPACT RESPONSE OF FLUID-SATURATED GRANULAR BEDS AND DENSE SUSPENSIONS

Neil A. Causley
Lieutenant, United States Navy
BE, SUNY Maritime College, 2013

Submitted in partial fulfillment of the
requirements for the degree of

MASTER OF SCIENCE IN PHYSICS

from the

NAVAL POSTGRADUATE SCHOOL
June 2020

Approved by: Abram H. Clark IV
Advisor

Emil P. Kartalov
Second Reader

Kevin B. Smith
Chair, Department of Physics

THIS PAGE INTENTIONALLY LEFT BLANK

ABSTRACT

Systems of sub-millimeter solid particles immersed in a simple fluid can exhibit a dramatic increase in flow resistance when they are rapidly sheared, often called discontinuous shear thickening (DST). A related process is impact-induced solidification, which occurs when an intruder is driven into a particle-fluid mixture. The resultant hardening is sufficient to dampen the movement of the intruder to essentially stop it in a distance much shorter than it would in other fluids. However, the fundamental physical processes that give rise to these behaviors are not well understood. An improved description would have several military applications, such as under-vehicle armor and pipe jacketing. It also could provide a better understanding of how mines interact with wet soils. This thesis presents a fundamental experimental and theoretical study of low-speed impacts into systems of glass beads of varying sizes mixed with water. Our results show that current models fail to capture many aspects of the behavior (e.g., how the peak stresses during impact depend on the initial impact speed and the particle diameter), suggesting that new theoretical descriptions are needed.

THIS PAGE INTENTIONALLY LEFT BLANK

Table of Contents

1 Introduction **1**

2 Background **3**
2.1 Microscopic Mechanisms 3
2.2 Impact Models 5
2.3 Summary 11

3 Experimental Methods **13**
3.1 Saturated Granular Bed Experiments 13
3.2 Dense Suspension Experiments. 15
3.3 Refractive Index Matching. 17

4 Experimental Results and Analysis **21**
4.1 Granular Bed Results. 21
4.2 Dense Suspension Results 25

5 The Added Mass Model **29**
5.1 Dependence on the Growing Mass 29
5.2 Simulation Methods 30
5.3 Results 31
5.4 Conclusion. 35

6 Conclusions **39**

List of References **41**

Initial Distribution List **43**

THIS PAGE INTENTIONALLY LEFT BLANK

List of Figures

Figure 2.1 Experimental set-up for the Waitukaitis and Jaeger tests of impact into dense suspensions. Source: [2]. 6

Figure 2.2 Illustration of velocity front and jamming of particles from a moving rod impacting suspended particles. Source: [2]. 7

Figure 2.3 Radial surface depression by impactor in the Waitukaitis and Jaeger experiment. Source: [2]. 8

Figure 2.4 An illustration of the proposed shape of the added mass after impact for a dense suspension. Source: [2]. 8

Figure 2.5 Experimental set-up for the Jerome et. al tests of impacts into granular beds. Source: [3]. 9

Figure 2.6 Impact of an intruder into photoelastic discs in the Krizou experiment. Source: [10]. 11

Figure 3.1 Intruder and accelerometer used in impact experiments. 14

Figure 3.2 Top: Examples of a granular bed in the container used for drop testing. Bottom: Overview of experimental rig, including camera and magnetic drop mechanism. 15

Figure 3.3 Left: Borosilicate microspheres floating in a very dense SPT-water mixture versus microspheres settled in a less dense mixture. Right: A density-matched SPT-water mixture containing soda-lime microspheres. 18

Figure 3.4 Top Left: A simplified drawing of a refractive index matching scanning (RIMS) setup (Source: [16]).Top Center: Top-down view of a laser sheet through a mixture of SPT-water and borosilicate microspheres. Top Right: A prepared sample of dense suspension with a laser being shined through. Bottom: Comparison of a control test (air only) and transmission through the dense suspension. 19

Figure 4.1 Left: Raw data from a 1-centimeter drop into a granular bed. Right: Zoomed-in image of the same data. Right: Zoomed-in and annotated selection of data from a 1-centimeter drop into a granular bed. . . 22

Figure 4.2 Position, acceleration, and velocity versus time for an intruder in a granular bed. 22

Figure 4.3 Left: Smoothed force data for a granular bed of 53-75 micron glass microspheres. Right: Smoothed force data for a granular bed of 600-850 micron glass microspheres. 23

Figure 4.4 Maximum force versus impact velocity for all granular bed experiments. The 53-75 μm microspheres are represented by red squares, 75-106 μm microspheres are the cyan asterisks, 180-212 μm microspheres are the black asterisks, 300-425 μm microspheres are the blue circles, and 600-850 μm microspheres are the black stars. . . 23

Figure 4.5 Scaling factor A versus mean microsphere diameter where the 53-75 μm microspheres are represented by a red square, 75-106 μm microspheres is the cyan asterisk, 180-212 μm microspheres is the black asterisk, 300-425 μm microspheres is the blue circle, and 600-850 μm microspheres is the black star. The dashed line represents the diameter dependence of the proportionality constant A in the equation $F_{\max} \propto Av^b$, and, in this case, is $1/d$. 24

Figure 4.6 Examples of force duration on impactor for 75-106 μm (left) and 300-425 μm (right) microspheres. 25

Figure 4.7 Left: Time to half-maximum force as a function of impact velocity for all grain sizes. Right: Total time between the first half-maximum and the second half-maximum as a function of impact velocity for all grain sizes. 53-75 μm microspheres are represented by red squares, 75-106 μm microspheres are the cyan asterisks, 180-212 μm microspheres are the black asterisks, 300-425 μm microspheres are the blue circles, and 600-850 μm microspheres are the black stars. . . 25

Figure 4.8 Left: Raw accelerometer data for a 1-centimeter drop into a dense suspension consisting of 75-90 μm borosilicate microspheres. Right: Raw accelerometer data for a 15-centimeter drop into the same. . 26

Figure 4.9 Left: Smoothed force data for a 1-centimeter drop into a dense suspension consisting of 75-90 μm borosilicate microspheres. Right: Smoothed force data for a 15-centimeter drop into the same. . . . 26

Figure 4.10 Maximum force versus impact velocity for all dense suspension experiments. Red squares reflect good data, blue asterisks reflect suspect data, and black circles reflect highly unreliable data. 27

Figure 4.11 Maximum force versus impact velocity for dense suspension experiments. Red circles represent the cornstarch data, red squares reflect good data, blue asterisks reflect suspect data, and black circles reflect highly unreliable data. 28

Figure 5.1 Left: Acceleration and velocity versus time from the Waitukaitis added mass model. Source: [2]. Center, Right: Acceleration and velocity versus time from simulations. 30

Figure 5.2 Acceleration and velocity versus time for 2D and 3D hemispherical added mass profiles for light masses with an α of zero. 32

Figure 5.3 Plots for all masses and an α of 1 numerically solved using the Waitukaitis model. Symbols in order of ascending M are circle, square, pentagram, triangle. 33

Figure 5.4 Plots for all masses and an α of 0 and a semi-circle/hemispherical added mass profile. Red colors represent the 2D added mass shape, black colors represent the 3D added mass shape, and symbols in order of ascending M are circle, square, pentagram, triangle, asterisk. . 34

Figure 5.5 Plots for all masses and an α of 0 and a rectangular/columnar added mass profile. Red colors represent the 2D added mass shape, black colors represent the 3D added mass shape, and symbols in order of ascending M are circle, square, pentagram, triangle, asterisk. . . 35

Figure 5.6 Plots for all masses and an α of 0 and a triangular/conic added mass profile. Red colors represent the 2D added mass shape, black colors represent the 3D added mass shape, and symbols in order of ascending M are circle, square, pentagram, triangle, asterisk. . . 36

THIS PAGE INTENTIONALLY LEFT BLANK

List of Tables

Table 5.1 Forms of $m_a(t)$ used in the differential equation solver to find dv/dt. 32

THIS PAGE INTENTIONALLY LEFT BLANK

Acknowledgments

First, I want to express my gratitude to my advisor, Professor Abe Clark, for his hard work and dedication. I also want to acknowledge Professor Joshua Dijksman of Wageningen University for his assistance in constructing the drop rig, data-collection program, and instruction on refractive index matching. His visit to NPS under Office of Naval Research Global Visiting Scientist Program VSP 19-7-001 and Office of Naval Research grant no. N0001419WX01519 was invaluable to our experiment. Lastly, I want to thank my wife, Kimberly, for her patience and support.

THIS PAGE INTENTIONALLY LEFT BLANK

CHAPTER 1:
Introduction

Impact-driven solidification is a phenomenon that occurs when an impactor is driven into a dense suspension of micrometer-sized particles. When the stresses are significant, the resultant hardening is sufficient to dampen the movement of the impactor to essentially stop it in a distance much shorter than it would in other fluids. Shear thickening is a similar and closely related steady-state phenomenon that occurs in dense suspensions. The potential for military applications for these kinds of phenomena range from under-vehicle armor to pipe jacketing, and enhancing our understanding of how these phenomena occur may allow us to exploit them for military use. This thesis reviews current literature in the field of dense suspensions, analyzes simulated and experimental data, and attempts to provide a new model for how the velocity front propagates through the suspension.

Chapters in this thesis are as follows:

1. Introduction
2. Background
3. Experimental Methods
4. Experimental Results and Analysis
5. Dependence on the Growing Mass
6. Conclusions

THIS PAGE INTENTIONALLY LEFT BLANK

CHAPTER 2:
Background

Discontinuous shear thickening (DST) is an effect where suspensions exhibit typical properties of liquids at low shear rates, but resistance to flow increases discontinuously with shear rate when sheared faster [1]. A large variety of particles and fluids interact this way and is thus inferred to be a generic characteristic of dense suspensions. Maharjan et al. found in a 2018 experiment that the steady-state rheology of DST does not explain the impact response of a cornstarch and water suspension [1]. The measured stresses present in the rheological tests were far lower than the measured stress under impact. They determined that they cannot explain the impact response using the same viscosity function as steady-state shear thickening in a rheometer. Additionally, they determined that this difference could not be explained by impact models based on added mass or other inertial effects.

The above results suggest that the relationship between impact-driven solidification and DST is not clear. Impact is a complex mixed-mode deformation including both shear and compression forces. Research into the mechanism of solidification has resulted in several theories, but a consensus has not been established on how exactly the force of an impactor propagates through the suspension or what force is experienced by the impactor. Waitukaitis and Jaeger suggest a model where the impact is an inelastic collision with a growing mass [2]–the "added mass model." Jerome, Vandenberghe, and Forterre [3] suggest a model where the solidification response depends on the interstitial pore pressure between particles–the "pore pressure model." The added mass and pore pressure models, however, still do not fully explain the response of a dense suspension that exhibits impact-driven solidification effects.

2.1 Microscopic Mechanisms

A number of different mechanisms are thought to affect shear- or impact-induced solidification, including Reynolds dilatancy [4], Darcy flow [5], particle jamming [6], lubrication between contacts [7], and the organic structure of the particle itself [8].

Reynolds dilatancy describes the tendency of granular media to change volume in response

to a shear deformation. Every change in stress that causes a change in position of grains causes a change of volume, a dilation or compaction. This occurs because grains that are hard cannot compress, nor go through one another, and must instead go around their neighbors. A sufficient amount of grains all doing this simultaneously in a volume of granular media causes the overall volume to dilate as the grains "flow" around each other in response to the external stress.

Darcy flow refers to how a fluid travels through a porous medium. The Darcy equation, $q = -\frac{k}{\mu}\Delta p$ relates flow rate (q) to permeability (k), viscosity (μ), and a pressure gradient (Δp) [5]. A volume of suspension can be thought of as many individual pores between grains. The viscosity is constant in the volume, and the space between grains is the permeability and scales like diameter squared. Smaller grain size effectively results in lower permeability and a lower flow rate. The inverse should also be true for larger grain sizes.

Jamming is case of liquid-solid transition when volume fraction ϕ is varied. Systems that exhibit Reynolds dilation–as well as all systems discussed in this thesis–have particle phases near their jamming point, and the fluid between particles is irrelevant. A small compression of a system near jamming will quickly induce solidification, but not due to fluid effects, instead strictly due to the interactions between particles. Discontinuous shear thickening occurs just below some critical packing fraction ϕ_c where jamming would occur and is referred to as a dynamically jammed state.

Lubrication forces cannot support the stresses of discontinuous shear thickening and the particles would interact as if they are undergoing solid-to-solid contact [6]. Effective viscosity in a fluid is determined by the equation $\eta = C\eta_l(a/h)$ where η_l is the liquid viscosity, a is particle diameter, the gap between particles is h, and C is a constant of order 1. If the gap becomes very small, on the order of two molecular layers, and the particle diameter is also very small, on the order of 14 μm as in cornstarch, one would expect the effective viscosity to be 4×10^4 that of water. However, experimentally measured suspensions of cornstarch in water have had effective viscosities of 10^7 times the viscosity of water.

Another factor is the particles' organic structure [8]. The fluid in which the particles are suspended also affect the suspension rheology, as in replacing water with ethanol. Performing this replacement causes the suspension to become a shear-thinning fluid rather than a shear-thickening fluid. Cornstarch is extremely hygroscopic, resulting in minimal

particle-liquid surface tension and consequent shear thinning effects in water [6]. The result is that cornstarch remains as a hard particle in water where other powders would turn into a gel or a colloid. Additionally, stiffer particles contribute more significantly to jamming and therefore discontinuous shear thickening. Particle friction contributes to lowering the minimum packing fraction ϕ in a suspension where a jamming transition could occur, making DST more likely.

These are a few examples of the main microscopic mechanisms that occur in a suspension, however, there are other mechanisms that affect shear- or impact-induced solidification as well. Generally, these are the most-researched effects but we still do not understand which are the most important and govern the overall behavior exhibited by these mixtures.

2.2 Impact Models

The goal of impact modeling is to build a simple model that incorporates one or more of the above mechanisms to capture the dominant behavior from impact experiments.

2.2.1 The Added Mass Model

The Waitukaitis added mass model is based on jamming and a slow relaxation time arising from a combination of the microscopic mechanisms described above. The experiment used in developing the added mass model involved an aluminum rod impacting the surface of a corn flour and water suspension at 1 m/s [2]. The packing fraction ϕ varied from 0.46 to 0.52. Acceleration of the rod was measured by an embedded accelerometer, and position and velocity measurements were made with a laser. A force sensor recorded stress experienced on the lower boundary directly under the rod. Figure 2.1 shows the locations of the accelerometer and force sensor, and provides a diagram of the experiment. Acceleration, velocity, and position of the rod were plotted against time, and the resultant plots were evaluated to find peak acceleration and the time it occurred.

Results

Jamming of particulates only occurs directly below the rod (Figure 2.2), and momentum is transferred to surrounding particles and forces them to move downward as well [2]. As seen in Figure 2.3, a depression forms radially from the site of impact. They determined

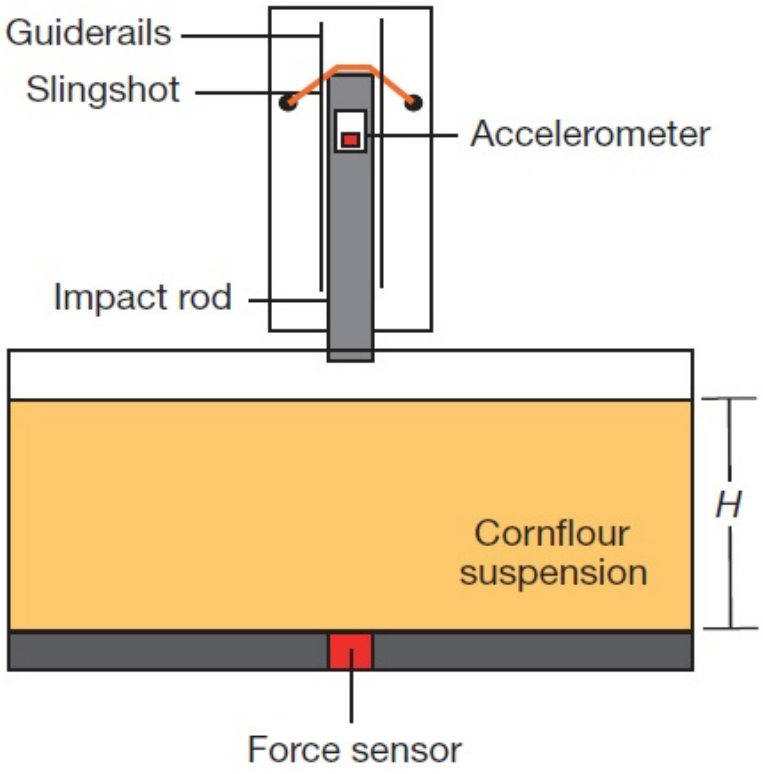

Figure 2.1. Experimental set-up for the Waitukaitis and Jaeger tests of impact into dense suspensions. Source: [2].

that the solid growth of mass is caused by the rod's motion [9], with the solidification front propagating at velocity $v_{\text{front}} = kv_{\text{rod}}$ where k is a constant that is approximately 12.2 [2]. They proposed that the growing mass, m_{a}, can be found via the force balance equation:

$$(m_{\text{rod}} + m_{\text{a}})a_{\text{rod}} = -(dm_{\text{a}}/dt)v_{\text{rod}} + F_{\text{ext}} \tag{2.1}$$

where F_{ext} includes gravity ($F_{\text{g}} = -m_{\text{rod}}g$) and the buoyant force. Using an approximation to estimate the size and shape of the growing mass region, they created a function for m_{a} for use in the Equation (2.1):

$$m_{\text{a}} = C(1/3)\pi\rho(r_{\text{rod}} + k|z_{\text{rod}}|)^2 k|z_{\text{rod}}| \tag{2.2}$$

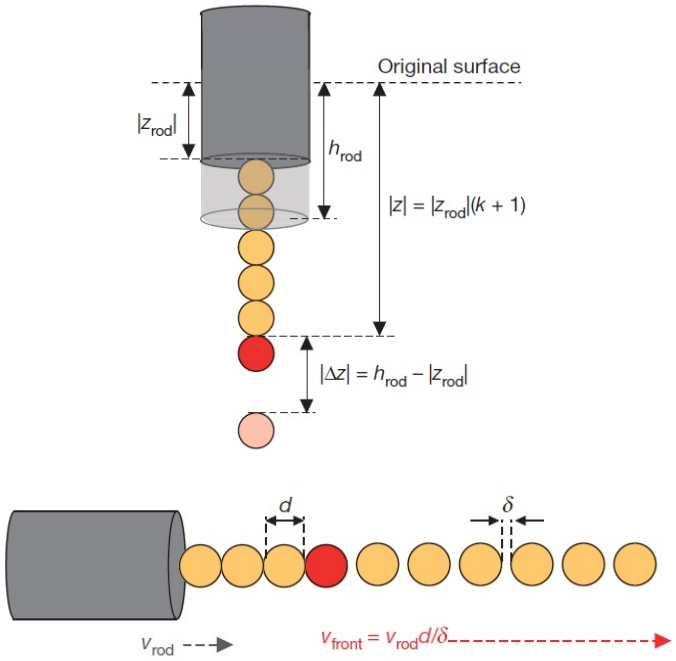

Figure 2.2. Illustration of velocity front and jamming of particles from a moving rod impacting suspended particles. Source: [2].

with initial conditions of $v_{\text{rod}}(0) = v_0$ and $z_{\text{rod}}(0) = 0$, where C is an added mass coefficient that is typically less than 1 [2].

An illustration (Figure 2.4) shows that a solidified region forms beneath the rod (red), an effective shape of added mass forms around the solidified region (orange), and the remaining volume of the suspension is unaffected (yellow). They conclude that their findings imply that impact resistance is proportional to jamming by compression of particles along the packing density (ϕ) axis. This jamming leads to a growing solid mass that drives flow around it, and the solid exhibits a yield stress and elastic properties [2]. Lastly, they show that the boundaries of the container are not the main factor in creating large normal stresses by varying the height of the suspension and finding their results did not change. This suggests the momentum that is transferred as the growing mass is pushed through the suspension by the impactor rather than the presence of boundaries [2].

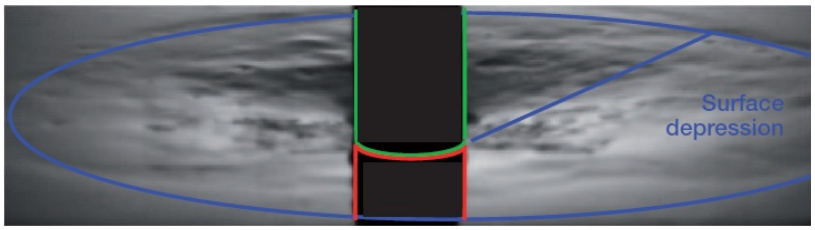

Figure 2.3. Radial surface depression by impactor in the Waitukaitis and Jaeger experiment. Source: [2].

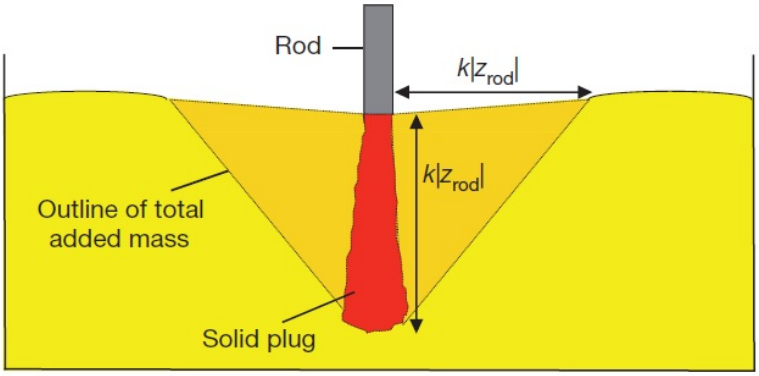

Figure 2.4. An illustration of the proposed shape of the added mass after impact for a dense suspension. Source: [2].

2.2.2 The Pore Pressure Model

The pore pressure model is based on Darcy flow and Reynolds dilatancy, and understanding the model requires explanation of how Darcy flow relates to granular suspensions. Darcy flow suggests that as the space between particles becomes smaller, resistance to flow increases and pressure increases. The pore pressure model attempts to explain impact behavior in suspensions using this relationship.

Experiment

Jerome et al. dropped a rigid glass sphere into a granular bed made of glass beads in the 0.1-1 mm range that were immersed in an incompressible fluid [3]. The initial packing fraction was controlled by fluidizing the mixture and compacting the sediment, then removing the excess liquid. Compacting the sediment was achieved by tapping the side of the container, and the number of taps applied controlled the packing fraction ϕ. They imaged each drop, and

took a high-frequency measurement of the interstitial fluid pressure inside the suspension directly under the impact. A diagram of their experimental set-up is shown in Figure 2.5. They varied impact speeds between 1.0 and 4.8 m/s, ϕ between 0.560 and 0.604, sphere diameter D between 16.5 and 25.2 mm, and sensor position z between 2 and 5 cm.

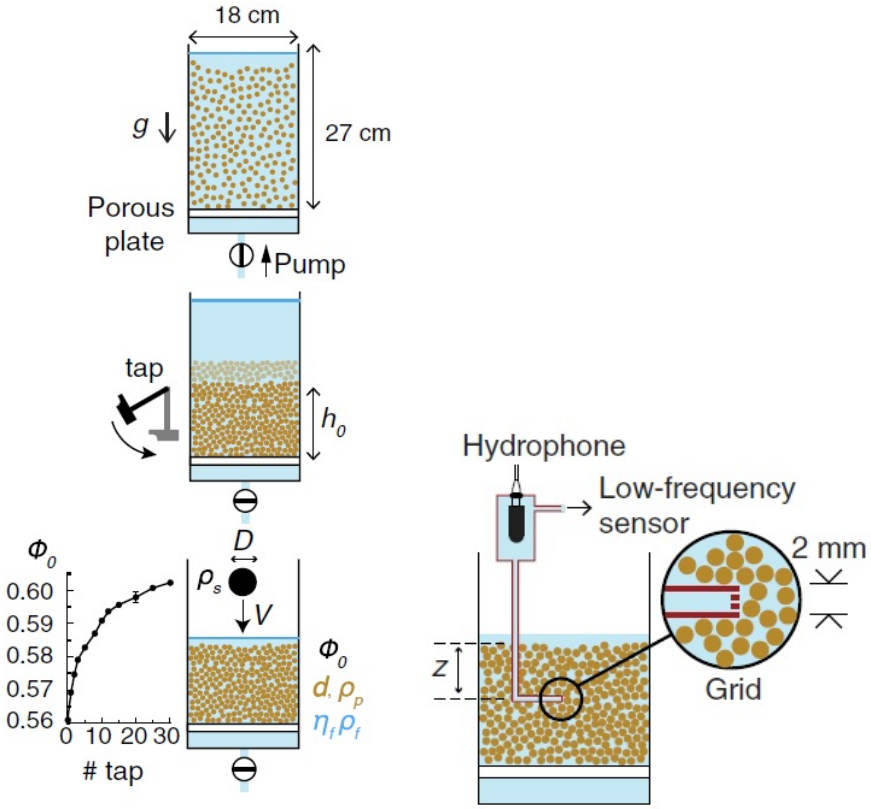

Figure 2.5. Experimental set-up for the Jerome et. al tests of impacts into granular beds. Source: [3].

Results

The experiment tested two cases; a "loose" case and a "dense" case [3]. In the loose case (ϕ = 0.560), the pore pressure shows a sudden positive peak after impact, and sometime after, sedimentation proceeds and the pressure relaxes to zero. This could be described as a Reynolds compaction. For the dense case (ϕ = 0.604), the peak pressure is negative. This indicated that particles are strongly pressed against each other, causing a solidification of the granular bed–described by Reynolds dilatancy. They found that the transition occurs for

a ϕ of approximately 0.585, and was independent of diameter D and impact velocity v. To model the pore pressure, they used the equation

$$P_f = -\frac{\eta_f}{\kappa}\alpha V_p(\phi - \phi_c)L \tag{2.3}$$

where V_p is the velocity scale for the particle velocity field, L is the extent to which deformation is experienced by the granular bed, and α is a constant of order 1. Importantly, κ is the permeability of the medium which is proportional to the diameter of the beads squared. This means that if the diameter is reduced by a factor of 10, the permeability is reduced by a factor of 100. Equation (2.3) shows that pore pressure is positive or negative depending on $\Delta\phi$, resulting in a fluid-like or solid-like response, respectively. The magnitude of the response is controlled by bead diameter and fluid viscosity.

Jerome et al. conclude that if $P_f \gg P_{\text{grav}}$, pore pressure excess dominates the impact dynamics and results in a quicksand-like or solid-like response based on the sign of $\Delta\phi$. If $P_f \ll P_{\text{grav}}$, the fluid pressure has a negligible contribution to inter-granular forces and results in the classical dry granular impact phenomenology [3]. They predict that forces should scale like $1/d^2$, but we find later that this does not seem to be the case in our experiments.

2.2.3 Power Law Scaling

Experiments and simulations performed by Krizou and Clark in a previous Naval Postgraduate School thesis indicate that added mass effects observed power law scaling in the initial stages of impacts into dry granular materials, but could not capture the forces experienced by the impactor [10]. Forces exerted on an intruder by grains are often well-described by using a velocity-squared drag force as in a Poncelet model, but initial impact forces are typically higher than expected. They performed experiments of impacts into photoelastic discs with Young moduli of 3 MPa, 23 MPa, and 360 MPa for soft, medium, and hard particles, respectively, and imaged the force propagation through the bed (Figure 2.6). The experiments revealed power law scaling for maximum force $F_{\text{max}} \propto v_0^{4/3}$ and $t_{\text{max}} \propto v_0^{-2/3}$, where t_{max} is the time at which maximum force was exerted on the intruder. Additionally, their results are not dependent on the initial packing fraction ϕ of the bed or the existence of friction. The conclusion is that shear-induced dilation and compaction do not affect the

scaling effects they measured.

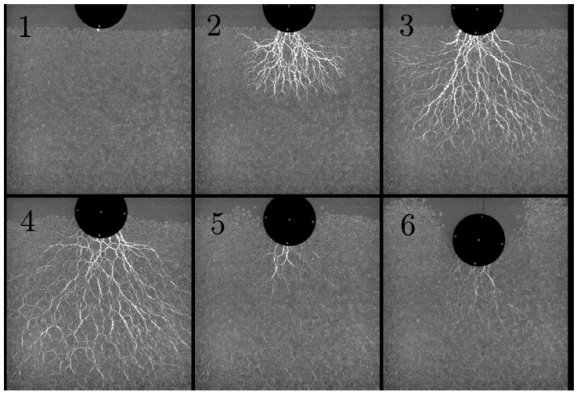

Figure 2.6. Impact of an intruder into photoelastic discs in the Krizou experiment. Source: [10].

Krizou suggests that an explanation of this power law scaling effect on maximum force on impacts into granular beds may be added mass effect, but current added mass models do not capture the observed scaling [10]. A mathematical form for added mass as a function of time, $m_a(t)$, may exist that will determine the trajectory of an intruder and $F_{\max}$. Figure 2.6 shows that a growing cluster of connected grains forms as the intruder of mass M impacts the bed, which is consistent with the added mass model. The form of $m_a(t)$ is dependent on 2D or 3D modeling: $\pi(v_f t)^2/2$ for 2D and $2\pi(v_f t)^3/3$ for 3D, where v_f is a constant. Solving this model gives $F_{\max} = Av_0$ in 2D and 3D rather than $F_{\max} \propto v_0^{4/3}$ where $A \propto M^{1/2}$ in 2D and $A \propto M^{2/3}$ in 3D. Additionally, $t_{\max}$ is independent of v_0 rather than proportional to $v_0^{-2/3}$.

2.3 Summary

The added mass model used jamming and a combination of Darcy flow and others to posit that the relaxation times are very slow, and a growing "added mass" dominates the deceleration. The added mass model also predicts maximum force versus impact velocity is quadratic [11]. The pore pressure model used Darcy flow and Reynolds dilatancy to predict force would be proportional to d^{-2}. Power law scaling is observed for dry impact experiments and added mass models, but there is some disagreement between the two.

This thesis describes work done experimentally and theoretically on impacts into particle-fluid systems that are either dense suspensions or saturated granular beds. We ask if cornstarch is special, or are we able to use inorganic materials to engineer these systems for Naval applications? Can relatively heavy glass microspheres be density or refractive index matched for experiments? Does particle size obey Darcy law predictions? How do added mass models scale with intruder size, mass, or dimension? How do these scalings compare to experimental results? We find that yes, glass microspheres can be used to recapture similar behavior as a cornstarch suspensions. Saturated beds deviate from the Darcy prediction outlined in the Jerome, et al. paper. Added mass models are characterized in Chapter V and compared to experimental data. Our results suggest that there are important deficiencies in the current models for describing the impact response of granular beds and dense suspensions.

CHAPTER 3:
Experimental Methods

Experiments involved testing both granular beds and dense suspensions of an incompressible fluid and glass microspheres. The intruder was constructed using a 20 millimeter diameter steel ball with a 5 centimeter protrusion used to attach an accelerometer (a similar configuration is pictured in Figure 3.1). The intruder assembly had a combined mass of 47 grams. The container used for the beds and suspensions was a plexiglass box with an area of 0.005 square meters (Figure 3.2). The experimental rig was controlled and the data was collected with LabView. An overview of the experimental rig can be seen in Figure 3.2. An electromagnet was connected to an adjustable platform to manipulate drop height and therefore impact velocity. Height measurements, and thus impact velocity, was measured from the top of the granular bed or suspension to the bottom of the steel ball using a standard ruler.

The experiment was recorded using a Phantom v711 high-speed camera recording at 150,000 frames per second. Intruder trajectories were plotted using a circular Hough transformation program in MATLAB. The accelerometer data and trajectory information were combined to form a detailed plot of intruder characteristics from its release to the point the Hough transformation could no longer track the sphere.

Experiments conducted using granular beds used tap water. Experiments conducted on dense suspensions used a density-matched mixture of tap water and sodium polytungstate (SPT-O) from GeoLiquids, Inc [12]. The microspheres were primarily soda lime glass, with some experiments performed using borosilicate glass. The microspheres were manufactured by the Mo-Sci Corporation and have a specific gravity of 2.2 and 2.5 grams per cubic centimeter for borosilicate and soda lime glasses, respectively [13], [14].

3.1 Saturated Granular Bed Experiments

Granular bed experiments were conducted using a variety of glass microsphere types and sizes, for a variety of drop heights. Testing was conducted using 600-850 micron soda lime microspheres, 300-425 micron soda lime microspheres, 180-212 micron borosilicate micro-

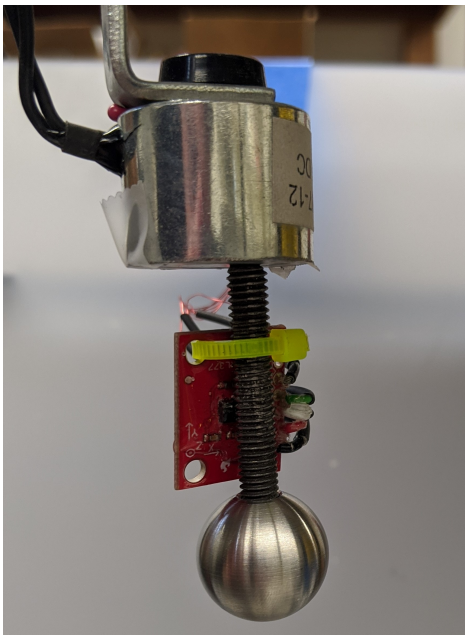

Figure 3.1. Intruder and accelerometer used in impact experiments.

spheres, 75-106 micron soda lime microspheres, and 53-75 micron soda-lime microspheres immersed in tap water with a thin layer of water above the granular bed. The 600-850 micron test used 150 milliliters of water and 574.85 grams of microspheres for a volume fraction ϕ of 0.6052. The 300-425 micron test used 150 milliliters of water and 554.6 grams of microspheres for a volume fraction ϕ of 0.5966. The 180-212 micron test used 100 milliliters of water and 313.95 grams of microspheres for a volume fraction ϕ of 0.5880. The 75-106 micron test used 100 milliliters of water and 358.4 grams of microspheres for a volume fraction ϕ of 0.5891. The 53-75 micron test used 100 milliliters of water and 358.25 grams of microspheres for a volume fraction ϕ of 0.5890.

Drop heights for the impactor varied from 1-20 centimeters. The accelerometer refresh rate was set to 5,000 Hz. Any crater or depression formed by an impact was removed before the following test by agitating the plexiglass box and allowing the mixture time to settle. Unlike the Jerome experiments, we did not tap the side of the box to encourage further packing of the microspheres.

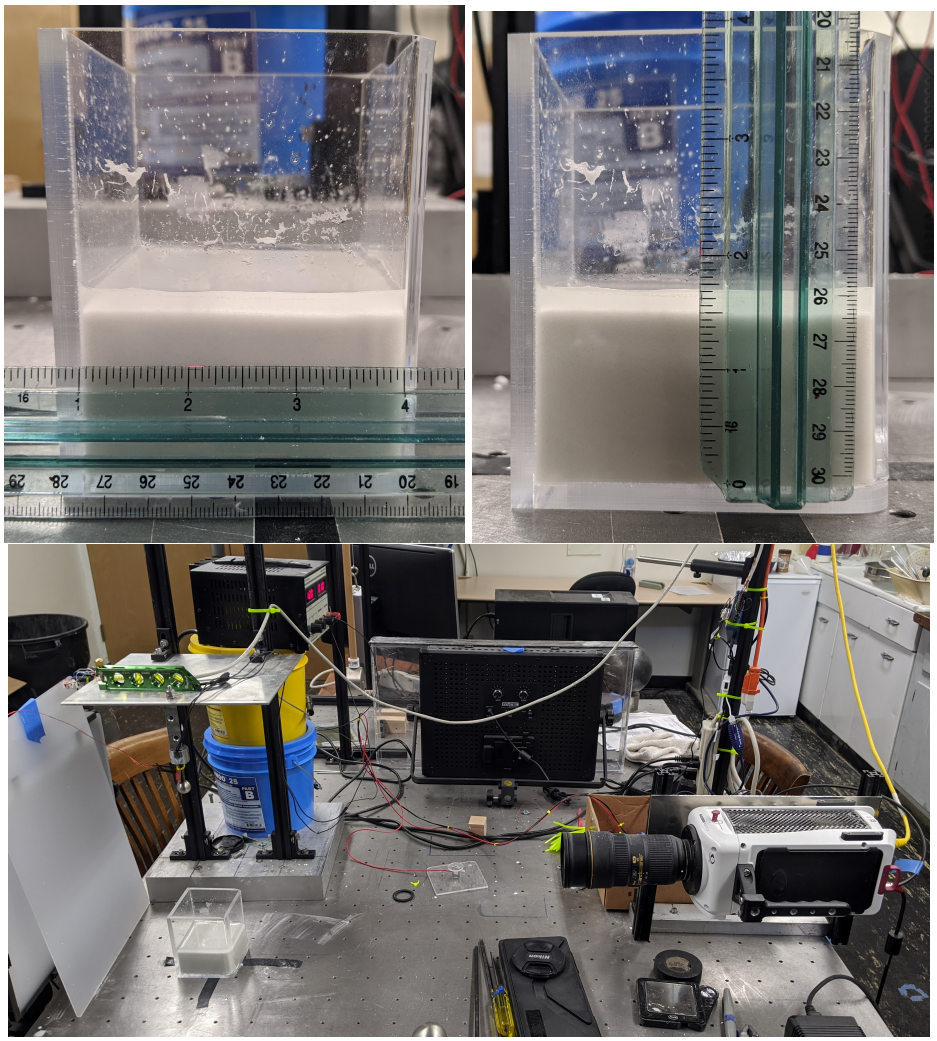

Figure 3.2. Top: Examples of a granular bed in the container used for drop testing. Bottom: Overview of experimental rig, including camera and magnetic drop mechanism.

3.2 Dense Suspension Experiments

Dense suspension experiments were performed using a sodium polytungstate (SPT) and water mixture and borosilicate or soda lime glass microspheres. The SPT mixture was created by measuring a set amount of water, and weighing the water. SPT was added while monitoring the weight of the solution. Once the weight was over 2 grams per milliliter, glass microspheres were added to the solution until they appeared to be neutrally buoyant with a settling time of two minutes or more. This process allowed us to closely match the fluid

density and microsphere specific gravity, creating a dense suspension.

Mass of the glass microspheres m_g can be determined by $\rho_g V_g$ where ρ_g is the glass density and V_g is the volume of microspheres. Similarly, mass of fluid (water) is $m_f = \rho_f V_f$. Since we have made a fluid where $\rho_f \approx \rho_g$, we can effectively exchange volume and mass in the equation for packing fraction ϕ:

$$\phi = \frac{V_g}{V_g + V_f} = \frac{m_g}{m_g + m_f} \tag{3.1}$$

The first small-scale experiment performed was to establish a density matched fluid to place the glass microspheres in. We began by placing 50 milliliters of water with mass of 48.95 grams in a beaker. We added a small amount of 75-90 micrometer borosilicate microspheres to test settling time as SPT was added to the water. We added 25 grams of SPT and stopped stirring the water, and observed the glass microspheres settling almost immediately. We added another 25 grams of SPT and stopped stirring the water, and observed the same behavior. We added another 25 grams of SPT, for a total of 75 grams added, and noted that it took approximately 2 minutes for the microspheres to settle in the solution. The final volume of the water and SPT mixture was 61 milliliters weighing 123.35 grams, for a density of 2.02 grams per milliliter. Further experiments used a similar ratio of SPT-to-water, but larger amounts of each to achieve the same density.

The next step was to manipulate the SPT-to-water ratio further, as well as manipulate the microsphere size and packing fraction. We also found that sufficient amounts of SPT could cause the fluid to become more dense than the microspheres, allowing them to effectively float on the mixture. A comparison of fluid density is shown in Figure 3.3.

The first packing fraction test used 75-90 micrometer borosilicate microspheres and small glass vials to establish an optimal packing fraction where the fluid exhibits characteristics typical of a dense suspension. We started with 200 microliters of SPT mixture weighing 3.928 grams. We used the above Equation (3.1) to calculate the weight of microspheres required to achieve a ϕ of 0.5, which was 3.928 grams. The actual amount added to the fluid was 4.019 grams, and the mixture was stirred. We did not notice any shear thickening effects at this ϕ as a reaction to stirring with a capillary tube. We proceeded to add more 75-90

micrometer microspheres to the mixture, calculating a total weight of microspheres of 4.801 grams to reach ϕ of 0.55. We added 0.787 grams of microspheres to the mixture, resulting in a ϕ of 0.55. Still, the mixture did not exhibit any shear thickening behavior when stirred. Lastly, we added an additional 1.09 grams of microspheres to the mixture. This resulted in a ϕ of 0.6, and the mixture did seem to exhibit shear thickening when stirred. The finished mixture in a vial can be seen in Figure 3.3. Overall, for a ϕ of 0.6, we used a total of 3.928 grams of SPT mixture and 5.896 grams of 75-90 borosilicate microspheres.

We used the same ratios and similar weights for soda lime microspheres in the 53-70 micrometer range and saw similar results. The soda lime microspheres were mixed with the SPT-water mixture above to make a range of density matched suspensions in the 0.5 to 0.6 ϕ range. We began with 3.894 grams of SPT-water solution, and added 3.9 grams of 53-70 microspheres for a ϕ of 0.5, and the mixture did not exhibit shear thickening behavior. In another vial, we used 3.97 grams of SPT-water solution and 4.849 grams of microspheres to achieve a ϕ of 0.55, and the mixture still did not exhibit shear thickening behavior. Lastly, we used 2.481 grams of SPT-water solution and 3.721 grams of 53-70 microspheres for a ϕ of 0.6 and the mixture did seem to exhibit shear thickening behavior. The rest times for all mixtures exceeded two minutes, indicating the density match between the solution and microspheres was near enough to conduct experiments.

3.3 Refractive Index Matching

A concept we wanted to explore in the course of our experiments with dense suspensions made with glass microspheres was refractive index matching (RIM). RIM is the process of combining particles and fluids with the same refractive index [15]. Previous experiments [15], [16] have been performed using refractive index matching scanning (RIMS) for hydrogels–soft particles that absorb water–and solids like glass. Joshua Dijksman provided us an overview of his technique and some "recipes" to start working towards imaging dense suspensions using index matching. His technique involves using a laser sheet to light a section of a volume of granular material as seen in Figure 3.4, imaging the volume, then using a computer to reconstruct the three-dimensional structure of the granular packing in the volume.

Our goal was to determine whether it was feasible to use a vertical, rather than horizontal,

Figure 3.3. Left: Borosilicate microspheres floating in a very dense SPT-water mixture versus microspheres settled in a less dense mixture. Right: A density-matched SPT-water mixture containing soda-lime microspheres.

laser sheet in an index-matched dense suspension of glass microspheres to take a live video of an impact. The laser used in our experiments was a 5 mW red laser with a wavelength of 630-643 nm from Osela, Inc. We used Nile Blue 690 perchlorate from Luxottica dissolved in ethanol at a 500:1 ratio to make a shelf-stable dye mixture. This had the added effect of requiring a small amount that has a negligible impact on the refractive index, and the ethanol evaporates under most conditions [16]. Nile Blue 690 perchlorate possesses a peak absorption wavelength of 633 nm and emission wavelengths of 650-690 nm, which is within the wavelengths provided by the laser we used. The amount of dye in a RIM liquid provides fluorescence and contrast between the dark particles and light fluid, however, absorption prevents the laser from penetrating deeply into the volume proportional to $exp(-\rho x)$ where x is the distance from the source and ρ is the dye concentration. It is also possible to tune the refractive index and quality of laser transmission by adding water or laser dye, respectively.

The refractive index of the borosilicate microspheres we used was 1.47-1.48, and we were able to achieve a similar refractive index in our SPT-water and microsphere mixture. We used 92 milliliters of deionized water, 25 grams of borosilicate microspheres, and 175.4

grams of sodium polytungstate with 6 microliters of Nile Blue 690-ethanol solution to make a sample. When we illuminated the mixture with the laser, we observed a beam width of approximately 0.125 inches after passing through the mixture, and measured a refractive index of 1.4771. Figure 3.4 shows the effects of fluorescence decay across the volume of fluid, Figure 3.4 shows a diagram of the test we performed, and Figure 3.4 shows a comparison of beam width between a control test in air versus the beam width after passing through the fluid.

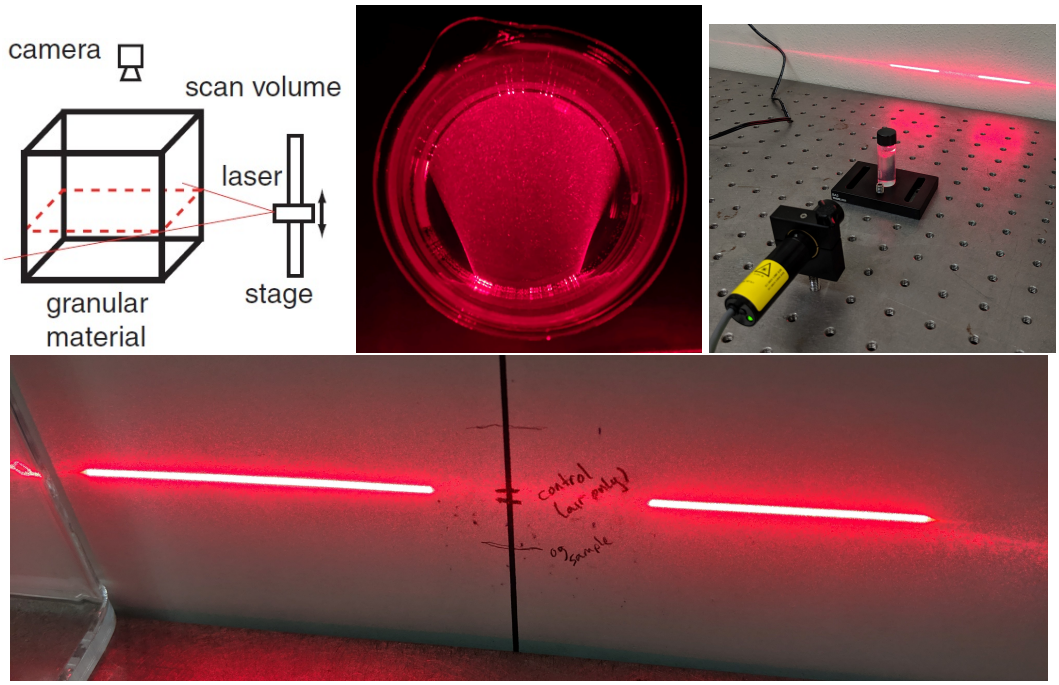

Figure 3.4. Top Left: A simplified drawing of a refractive index matching scanning (RIMS) setup (Source: [16]).Top Center: Top-down view of a laser sheet through a mixture of SPT-water and borosilicate microspheres. Top Right: A prepared sample of dense suspension with a laser being shined through. Bottom: Comparison of a control test (air only) and transmission through the dense suspension.

The recipes used and formulations described in the Sections above are highly reproducible and, should a student choose to, can be applied immediately to any new research in the field of granular impacts, dense suspensions, or refractive index matching.

THIS PAGE INTENTIONALLY LEFT BLANK

CHAPTER 4:
Experimental Results and Analysis

This Chapter shows analysis and results of impacts into saturated granular beds and dense suspensions. We find that Darcy flow does not capture effects of impacts into granular beds, and that a dense suspension consisting of glass microspheres exhibits behavior and forces similar to cornstarch.

4.1 Granular Bed Results

Raw data for impacts into granular beds was provided by an accelerometer recording 5,000 samples per second. The accelerometer records on three channels, but since it is a purely vertical drop, we would select only the vertical channel. Figure 4.1 shows the three channels, with the blue line being the vertical channel of interest. The deflection to the left of the peak is due to being released from the drop rig, and corresponds with gravitational acceleration. Total deceleration due to impact is measured from the bottom of the peak to the top. When we process the acceleration data, we only select points from the bottom of the peak to when the accelerometer returns to zero, as seen in the right section of Figure 4.1. Additionally, we plot position, velocity, and acceleration as functions of time as seen in Figure 4.2

We then took the raw acceleration data, applied a low-pass filter to reduce noise, and multiplied by intruder mass to find peak force exerted on the intruder. Figure 4.3 shows an example of the smoothed force data for a granular bed of 53-75 and 600-850 micron microspheres. Peak force is found at the vertex of the curve produced by this smoothed accelerometer data multiplied by intruder mass.

In order to form a comparison to the pore pressure model, we need to examine how peak force corresponds to grain size in the bed. All peak forces for all drop heights was plotted on the same chart (Figure 4.4). The horizontal axis represents maximum–and therefore impact–velocity of the intruder, and the vertical axis represents maximum force experienced by the intruder. The plot is a double-logarithmic plot. The dashed lines represent a weighted fit of the data. The 53-75 μm microspheres are represented by red squares, 75-106 μm microspheres are the cyan asterisks, 180-212 μm microspheres are the black asterisks, 300-

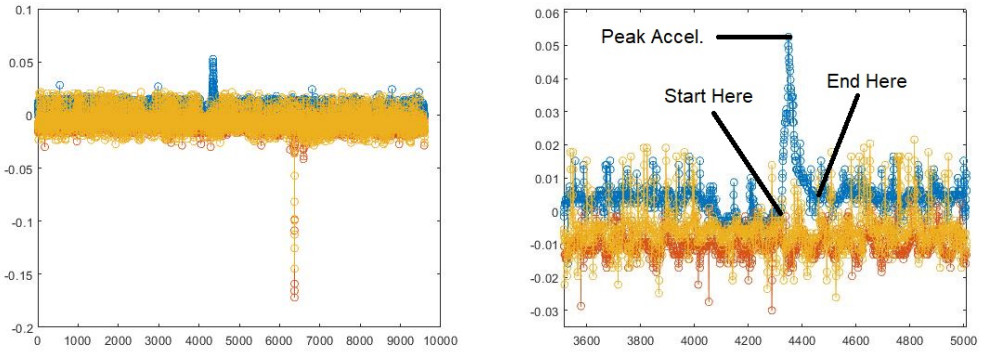

Figure 4.1. Left: Raw data from a 1-centimeter drop into a granular bed. Right: Zoomed-in image of the same data. Right: Zoomed-in and annotated selection of data from a 1-centimeter drop into a granular bed.

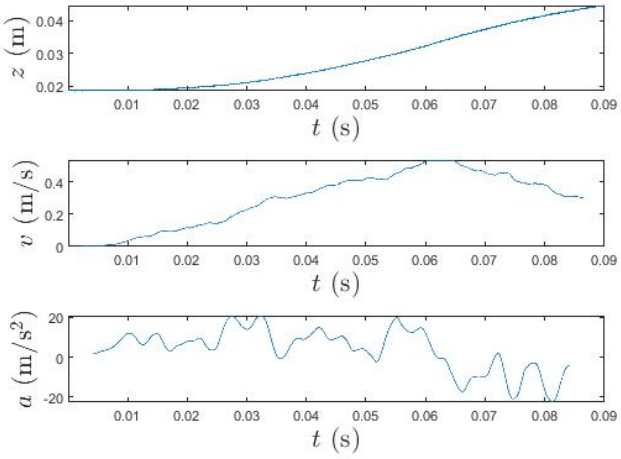

Figure 4.2. Position, acceleration, and velocity versus time for an intruder in a granular bed.

425 μm microspheres are the blue circles, and 600-850 μm microspheres are the black stars.

We know that if force was proportional to $1/d^2$ as is claimed by the pore pressure model, we would expect force to be approximately 100 times higher for the 53-75 μm microspheres than the 600-850 μm microspheres. Our results indicate that in actuality, forces scale approximately linearly with microsphere diameter. This raises the question, then, of how the

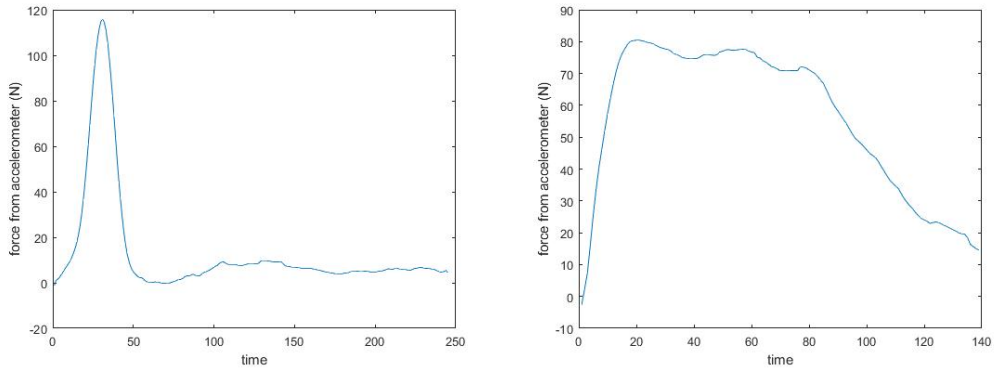

Figure 4.3. Left: Smoothed force data for a granular bed of 53-75 micron glass microspheres. Right: Smoothed force data for a granular bed of 600-850 micron glass microspheres.

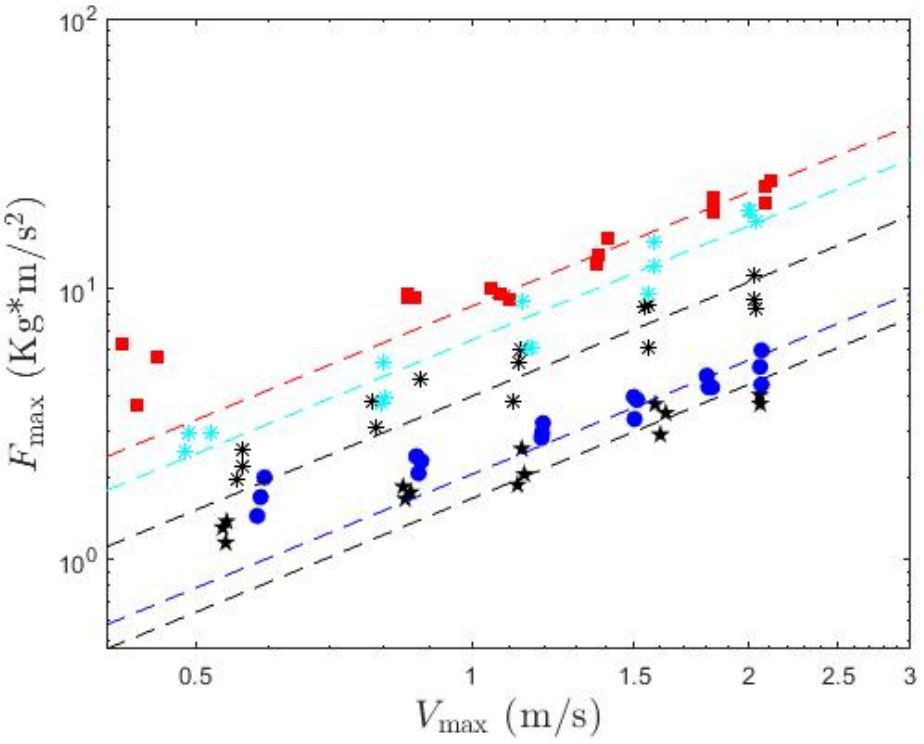

Figure 4.4. Maximum force versus impact velocity for all granular bed experiments. The 53-75 μm microspheres are represented by red squares, 75-106 μm microspheres are the cyan asterisks, 180-212 μm microspheres are the black asterisks, 300-425 μm microspheres are the blue circles, and 600-850 μm microspheres are the black stars.

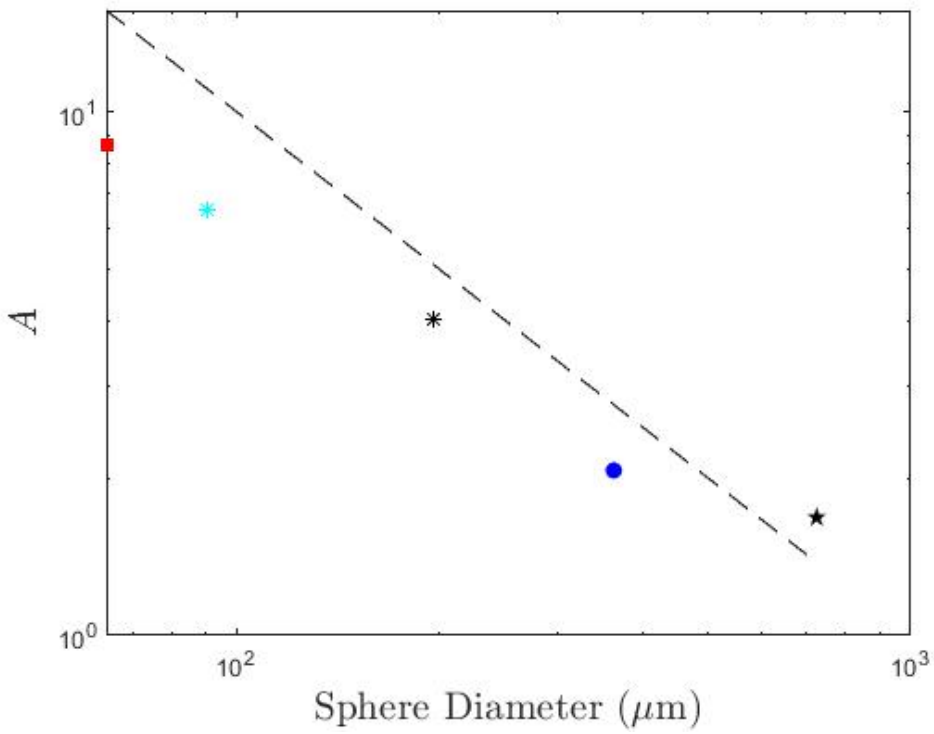

Figure 4.5. Scaling factor A versus mean microsphere diameter where the 53-75 μm microspheres are represented by a red square, 75-106 μm microspheres is the cyan asterisk, 180-212 μm microspheres is the black asterisk, 300-425 μm microspheres is the blue circle, and 600-850 μm microspheres is the black star. The dashed line represents the diameter dependence of the proportionality constant A in the equation $F_{\max} \propto Av^b$, and, in this case, is $1/d$.

results actually scale. Power law scaling suggests that maximum force $F_{\max}$ is proportional to Av^b [10]. When grain size is plotted against A in a log-log plot, the magnitude of the best fit curve–shown as a dashed line–would represent the proportionality constant A on grain diameter. Figure 4.5 shows that this is a line of slope approximately equal to -1, meaning A should contain a $1/d$ term. From the data seen in Figure 4.4, we see that $b \approx 1.4$.

In addition to the magnitude of force being dependent on grain size, we find that the duration in which the force is exerted is also dependent on grain size. The amount of time it takes to reach the first half-maximum of force does not seem to be correlated at all to impact velocity or microsphere size, as shown in Figure 4.7. However, the total duration over which

the force is exerted seems to be linearly related to velocity and grain size. Figure 4.3 is a typical example of the difference between first and second half-maximum times dependence on microsphere size.

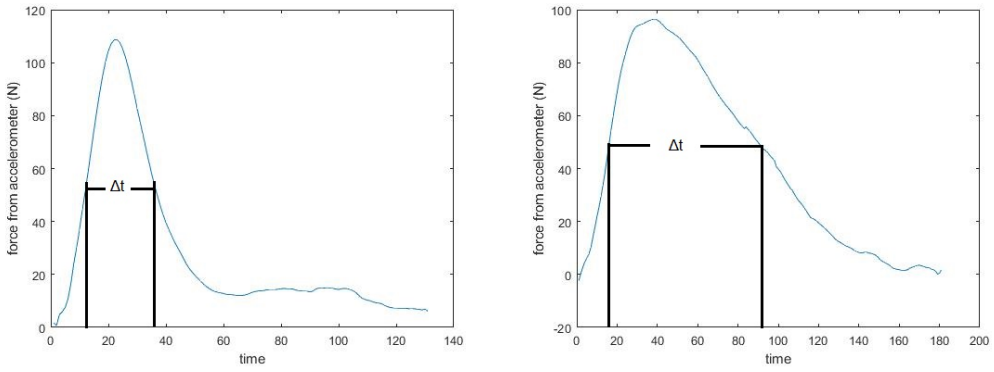

Figure 4.6. Examples of force duration on impactor for 75-106 μm (left) and 300-425 μm (right) microspheres.

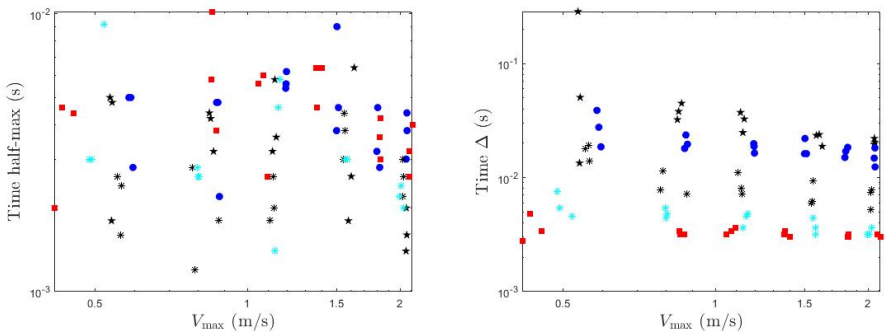

Figure 4.7. Left: Time to half-maximum force as a function of impact velocity for all grain sizes. Right: Total time between the first half-maximum and the second half-maximum as a function of impact velocity for all grain sizes. 53-75 μm microspheres are represented by red squares, 75-106 μm microspheres are the cyan asterisks, 180-212 μm microspheres are the black asterisks, 300-425 μm microspheres are the blue circles, and 600-850 μm microspheres are the black stars.

4.2 Dense Suspension Results

We used the same procedure as described in Section 4.1 to acquire and present the force and acceleration data for our dense suspension experiments. The experimental suspension

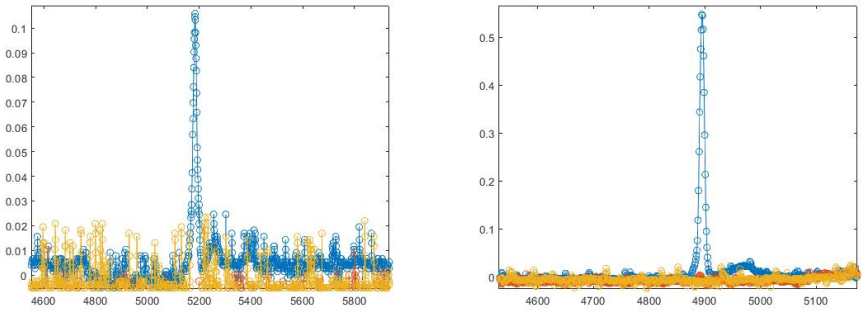

Figure 4.8. Left: Raw accelerometer data for a 1-centimeter drop into a dense suspension consisting of 75-90 μm borosilicate microspheres. Right: Raw accelerometer data for a 15-centimeter drop into the same.

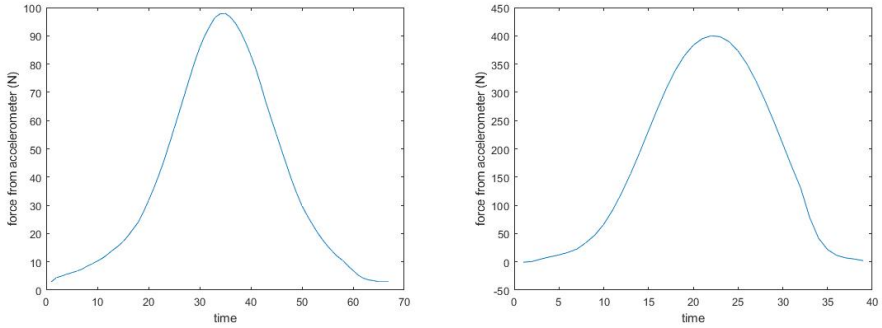

Figure 4.9. Left: Smoothed force data for a 1-centimeter drop into a dense suspension consisting of 75-90 μm borosilicate microspheres. Right: Smoothed force data for a 15-centimeter drop into the same.

consisted of 75-90 μm borosilicate microspheres and the density matched SPT solution. The mixture used 100 mL of SPT-water of mass 198.25 grams. We then added 297.35 grams of microspheres for a ϕ of 0.6, which was where DST "turned on" based on previous testing.

Data was recorded in the same manner as the granular bed experiments. Accelerometer data was clipped to only include the start of the impact through the end of the deceleration, and then multiplied by intruder mass and smoothed to form a curve (Figures 4.8, 4.9). An excessive amount of noise and a loose connection in the accelerometer had an adverse effect on some accelerometer data and the experiment was not able to be performed again due to concerns around COVID-19. Data that is suspect will be annotated in captions of figures and in the body of this thesis.

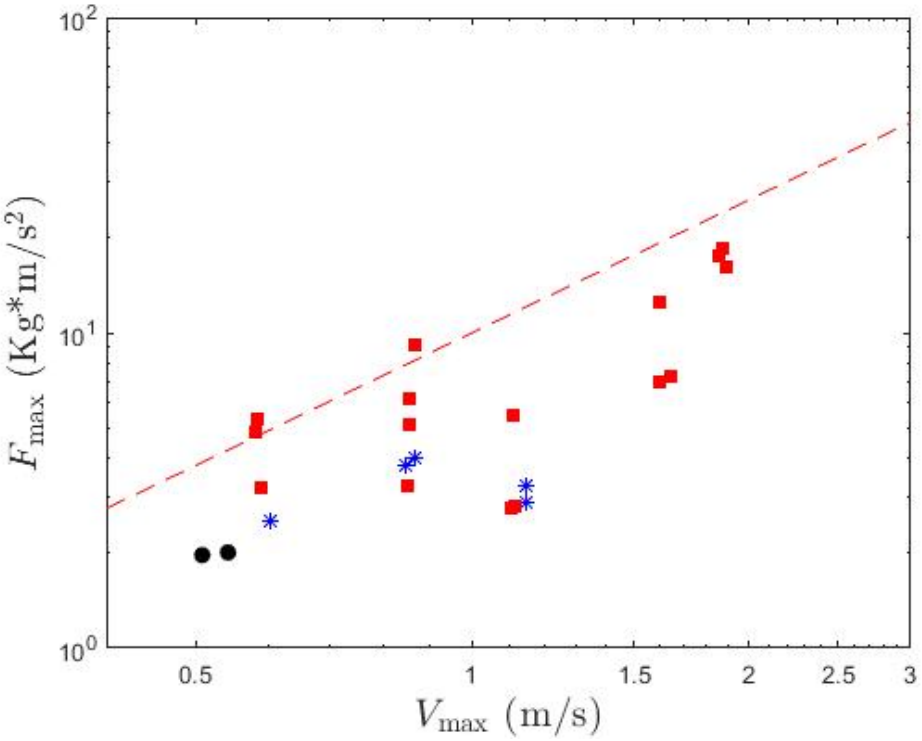

Figure 4.10. Maximum force versus impact velocity for all dense suspension experiments. Red squares reflect good data, blue asterisks reflect suspect data, and black circles reflect highly unreliable data.

Forces exerted on the intruder were on the same order as the forces seen in granular bed experiments for similar-sized microspheres. The range of forces for impact in dense suspensions is 2-11 kg·m/s^2, and the range of forces for 75-106 μm microspheres in a granular bed test was also from 2-11 kg·m/s^2. Figure 4.10 shows the maximum force exerted on the intruder plotted against impact velocity. It should be noted that the black circles are data that was determined as being highly unreliable, and the blue asterisks are data that was determined to be suspect.

Testing conducted on a dense suspension of cornstarch and water with an intruder of a similar mass yielded similar results. A test by Marc Brassard of NPS using a 20 millimeter sphere with a mass of 48 grams into a cornstarch result plotted against data using the same impactor with a mass of 50.5 grams can be seen in figure 4.11. It is apparent that for a similar intruder size, shape, and mass, the results are surprisingly similar. This result indicates that

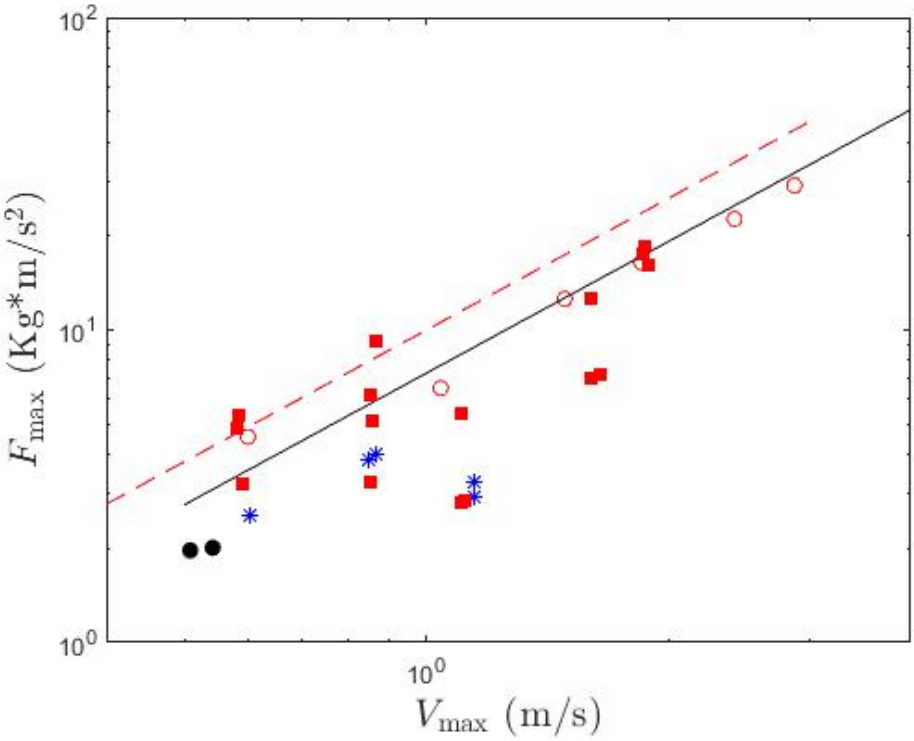

Figure 4.11. Maximum force versus impact velocity for dense suspension experiments. Red circles represent the cornstarch data, red squares reflect good data, blue asterisks reflect suspect data, and black circles reflect highly unreliable data.

perhaps organic structure, Reynolds dilatancy, and Darcy flow are not as important to the overall response of the suspension under impact as once thought. Cornstarch is nearly 9 times smaller in diameter than the borosilicate microspheres used in the experiment (14 μm versus 75-90 μm), and glass exhibits none of the same hygroscopic properties or roughness of shape that cornstarch does. Yet, much of the data of peak force versus impact velocity for borosilicate microspheres lies on the same line and has the same magnitude as cornstarch particles. This finding may be an interesting topic for a future thesis.

CHAPTER 5:
The Added Mass Model

Added mass models are commonly used [2], [9], [11], [17], [18], with 199 citations on the Waitukaitis paper alone. However, there has been no systematic study for how the peak forces and times in such a model depend on important system parameters like intruder speed, intruder mass, or dimensionality. This Chapter gives a characterization of the relationships between these quantities and the peak forces experienced by the impacting object.

5.1 Dependence on the Growing Mass

The governing equation behind the added mass model arises from Newton's second law of motion, $F = dp/dt$. Momentum, p, is defined as mass of an object multiplied by its velocity. Therefore, $F = d(mv)/dt$, and since in our model both mass and velocity are changing, we separate them into

$$F_{\text{ext}} = (M + m_a)\frac{dv}{dt} + v\frac{dm_a}{dt}, \tag{5.1}$$

where M is the mass of the intruder, m_a is the added mass, F_{ext} is the external forces, and v is the velocity of the intruder and the added mass. Added mass effects are also important in typical liquids like water [19], but are more pronounced in a suspension because the solidification under the impactor causes rapid growth of m_a and acts like a growing solid object [2].

The characteristic front speed v_f at which the added mass expands depends on the type of material undergoing the impact. Waitukaitis proposed a model based on volume conservation [2]. The plowing intruder sweeps out some volume over a time interval, and that volume must be equal to grains transitioning from not in contact to in contact. This suggests that the velocity of the front is proportional to the velocity of the impactor. Waitukaitis et al. found evidence supporting this, with $v_f \approx 12.2v$ as stated in Chapter 2 of this thesis [2]. Using the information found in the Waitukaitis paper, we constructed a MATLAB program that recreates the dynamics of an impact into a granular suspension and achieved similar results as shown in Figure 5.1.

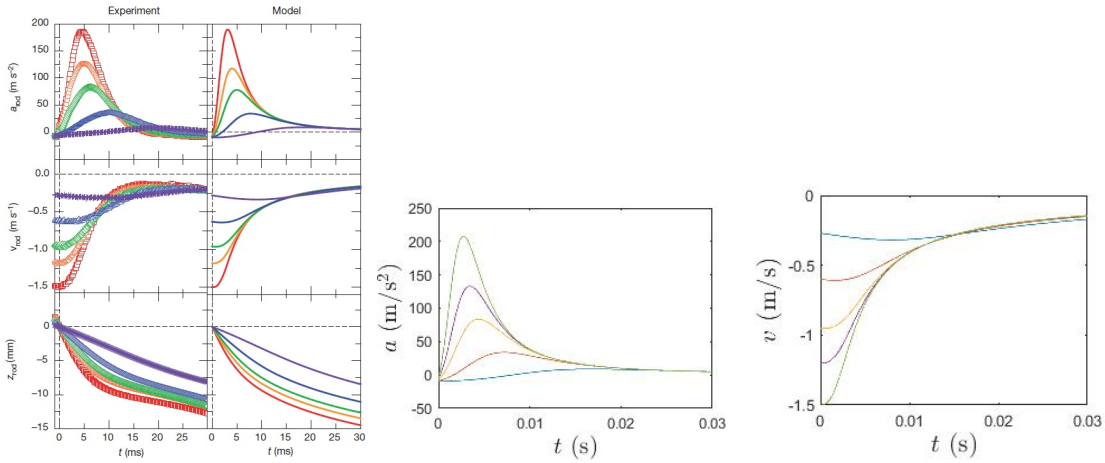

Figure 5.1. Left: Acceleration and velocity versus time from the Waitukaitis added mass model. Source: [2]. Center, Right: Acceleration and velocity versus time from simulations.

In addition to $v_f \propto v$ (or $v_f \propto v^\alpha$ with $\alpha = 1$), we also study constant v_f (or $v_f \propto v^\alpha$ with $\alpha = 0$) to try to more fully characterize the behavior of this class of model. For example, a dry granular material comprised of elastic spheres would have a front that propagated at a constant speed if not in the shock regime and $v_f \propto v^{1/5}$ if in the shock regime [20], [21].

Choosing a form of $m_a(t)$ and setting $F_{\text{ext}} = 0$ fully constrains the dynamics, and modifying other parameters in the $m_a(t)$ equation will result in changes to macroscopic measurements such as peak force during impact. The remainder of this Chapter is devoted to solving Equation (5.1) with various choices of m_a and characterizing how peak force and time depend on these choices.

5.2 Simulation Methods

Simulations were conducted using MATLAB R2020a. We first numerically solved the Waitukaitis added mass model, as in Equation (5.1). This has $\alpha = 1$ and an added mass shape of a growing conical-like structure, as shown in Figure 2.4. These simulations used a modified velocity Verlet integration scheme. Comparison with the numerical solutions from Waitukaitis [2] are shown in Figure 5.1. This is shown to verify our simulation gives approximately the same solutions as the published results. Note that the published results showed trajectories but not the dependence of $F_{\max}$ and $t_{\max}$ on v_0 and other parameters.

We also study a simplified version of an added mass model where $\alpha = 0$ and $F_{\text{ext}} = 0$. This corresponds to the regime where impact forces are dominant and the front velocity is constant. Physically, this would correspond to fast impacts into a material with a linear sound speed, which might be more relevant to dry elastic grains. However, we use it to uncover general rules about how added mass models behave. We also verify that setting $F_{\text{ext}} = 0$ does not substantially affect our results (for the Waitukaitis added-mass model or for the one discussed below with $\alpha = 0$).

The $\alpha = 0$ simulations used an ordinary differential equation solver that used an input of an added mass as it propagates through a fluid. The solver could be adjusted to produce two- or three-dimensional added mass shapes, a variety of impactor masses, a range of time intervals, and a range of initial impact velocities. Additionally, the diameter of the intruder D could be modified (if intruder diameter is relevant to the particular choice of added mass shape), and the speed at which the added mass front grows could be modified to represent different kinds of materials (e.g. a dry granular system or a dense suspension). The impactor masses ranged from 0.5 to 500, the impact velocities ranged from 10^{-1} to 10^{1}, and the typical time range necessary to see the full interaction was 10. In our case, we remove any dependence on gravity and buoyant force to isolate only the forces exerted on the intruder by the added mass interaction itself. Solving Equation (5.1) assuming $F_{\text{ext}} = 0$ for dv/dt results in

$$\frac{dv}{dt} = -v\frac{dm_a}{dt}/(M + m_a) \tag{5.2}$$

and forces exerted on the intruder can be determined by $M \cdot dv/dt$.

The shapes of 2D (3D) added mass used in our simulations determined the form of $m_a(t)$, and were circular (spherical), rectangular (columnar), or triangular (conal). The equations used for two- and three-dimensional added mass shapes are found in Table 5.1. The variable ρ_g was set to 1. Dimensionality of the growing mass is d. The program iterated over each dimension (2D or 3D), each mass, and each impact velocity.

5.3 Results

Results were plotted for acceleration against time, velocity against time, force against velocity, velocity against time, A against M, and B against M.

Shape	m_a	dm_a/dt	d
2D Circ.	$\frac{\pi}{2}\rho_g(v_f t)^2$	$\pi\rho_g v_f^2 t$	2
3D Sph.	$\frac{2}{3}\pi\rho_g(v_f t)^3$	$2\pi\rho_g v_f^3 t^2$	3
2D Rect.	$\rho_g D v_f t$	$\rho_g D v_f$	1
3D Col.	$\frac{\pi}{4}D^2\rho_g v_f t$	$\frac{\pi}{4}D^2\rho_g v_f$	1
2D Tri.	$\rho_g(v_f t)^2 + \frac{Dv_f t}{2}$	$2\rho_g v_f^2 t + \frac{Dv_f}{2}$	2
3D Cone	$\rho_g(\frac{\pi}{3}(v_f t + \frac{D}{2})^3 - \frac{D^3}{8})$	$\pi\rho_g v_f(v_f^2 t^2 + Dv_f t + \frac{D^2}{4})$	3

Table 5.1. Forms of $m_a(t)$ used in the differential equation solver to find dv/dt.

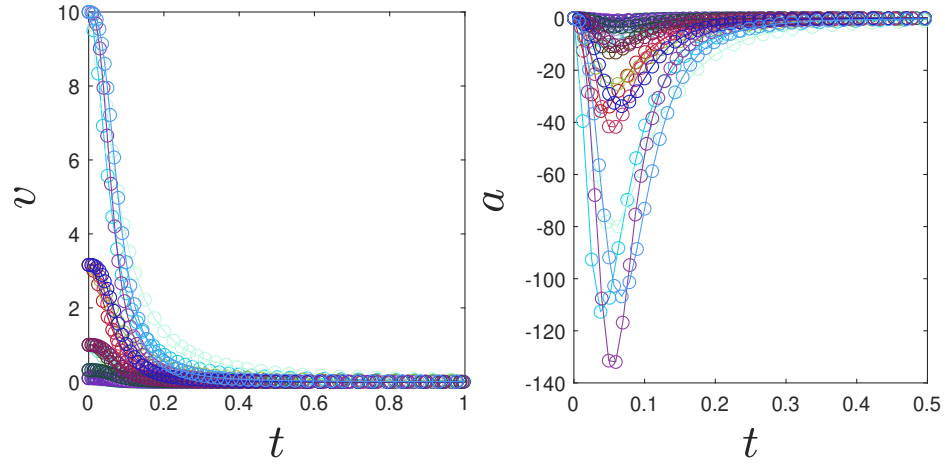

Figure 5.2. Acceleration and velocity versus time for 2D and 3D hemispherical added mass profiles for light masses with an α of zero.

5.3.1 Acceleration and Velocity

Results from numerically solving the Waitukaitis model using $M = 0.368$ is found in Figure 5.1. Results from light masses ($M = 0.1$ and $M = 1$) and α of 0 for a semi-circle and hemispherical simulation are found in Figure 5.2.

5.3.2 A, B, F, v Dependencies

Simulations for $\alpha = 1$ were performed using impactor masses M equal to 0.078, 0.1446, 0.227, and 0.368 kilograms. Symbols, in order of ascending M, are circle, square, pentagram, triangle. Numbers in the field of the plots represent the slope of the dashed line nearest

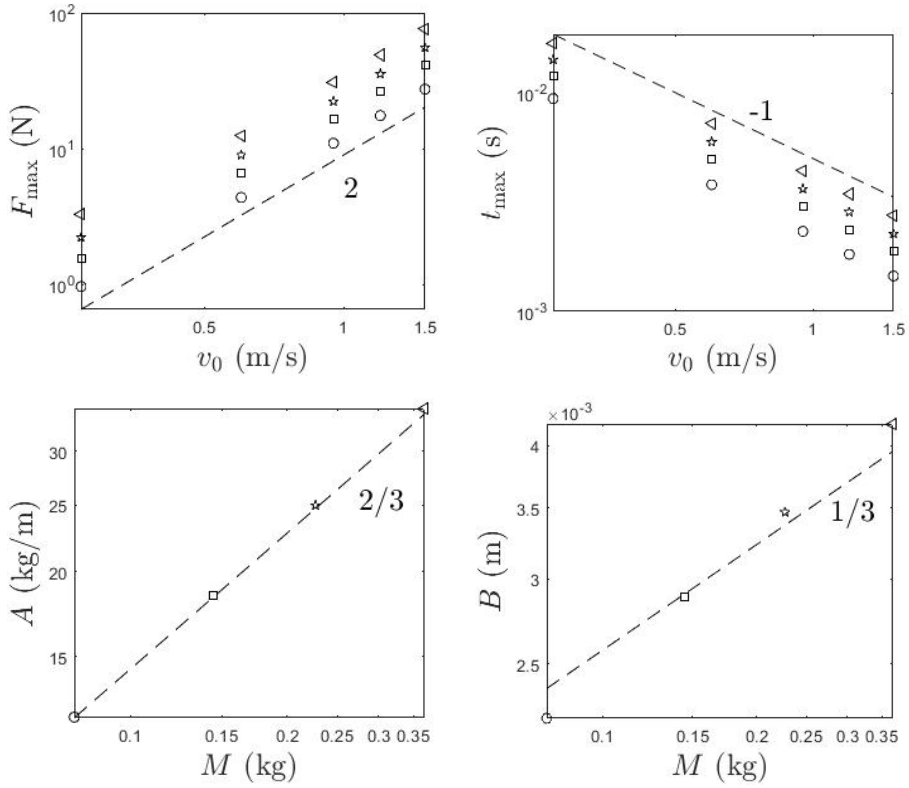

Figure 5.3. Plots for all masses and an α of 1 numerically solved using the Waitukaitis model. Symbols in order of ascending M are circle, square, pentagram, triangle.

them. All plots are double logarithmic plots.

Simulations for $\alpha = 0$ were performed using impactor masses M equal to 0.5, 1, 5, 50, 500. To simplify calculations, we assume a v_f that is constant over time and only affected by impact velocity scaled by a constant and α in the form of $v_f = kv^\alpha$. This simplifies the dynamics, and $m_a(t)$ and dm_a/dt become much simpler because now they are only time-dependent. For all plots, red colors represent the two dimensional added mass simulations and black colors represent the three dimensional simulations. Symbols, in order of ascending M, are circle, square, pentagram, triangle, asterisk. Numbers in the field of the plots represent the slope of the dashed line nearest them. All plots are double logarithmic plots.

Plots for all masses and an α of 0 and a semi-circle/hemispherical added mass profile are found in Figure 5.4. Plots for all masses and an α of 0 and a rectangular/columnar added

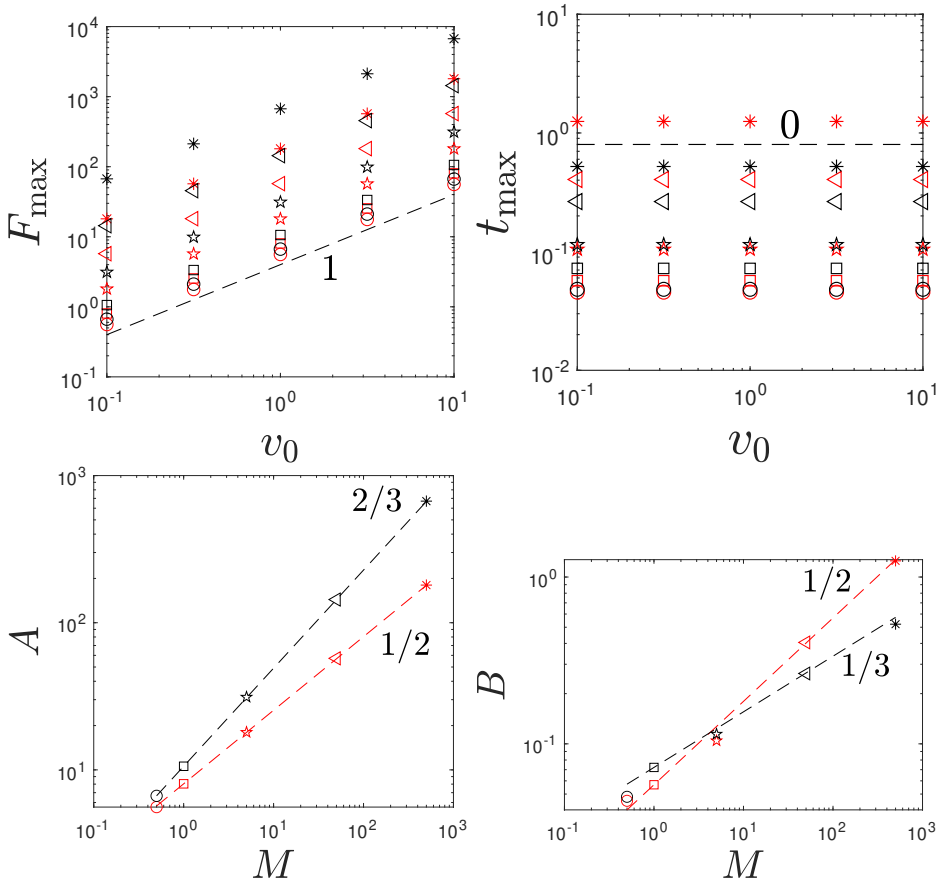

Figure 5.4. Plots for all masses and an α of 0 and a semi-circle/hemispherical added mass profile. Red colors represent the 2D added mass shape, black colors represent the 3D added mass shape, and symbols in order of ascending M are circle, square, pentagram, triangle, asterisk.

mass profile are found in Figure 5.5. Plots for all masses and an α of 0 and a triangular/conic added mass profile are found in Figure 5.6.

These plots indicate that peak force could be found by $Av_0^{1+\alpha}$. This relationship is not understood, but is a generic scaling equation that captures any variation of parameters that we performed. Additionally, other factors such as impactor diameter or mass do not matter as much as this scaling factor.

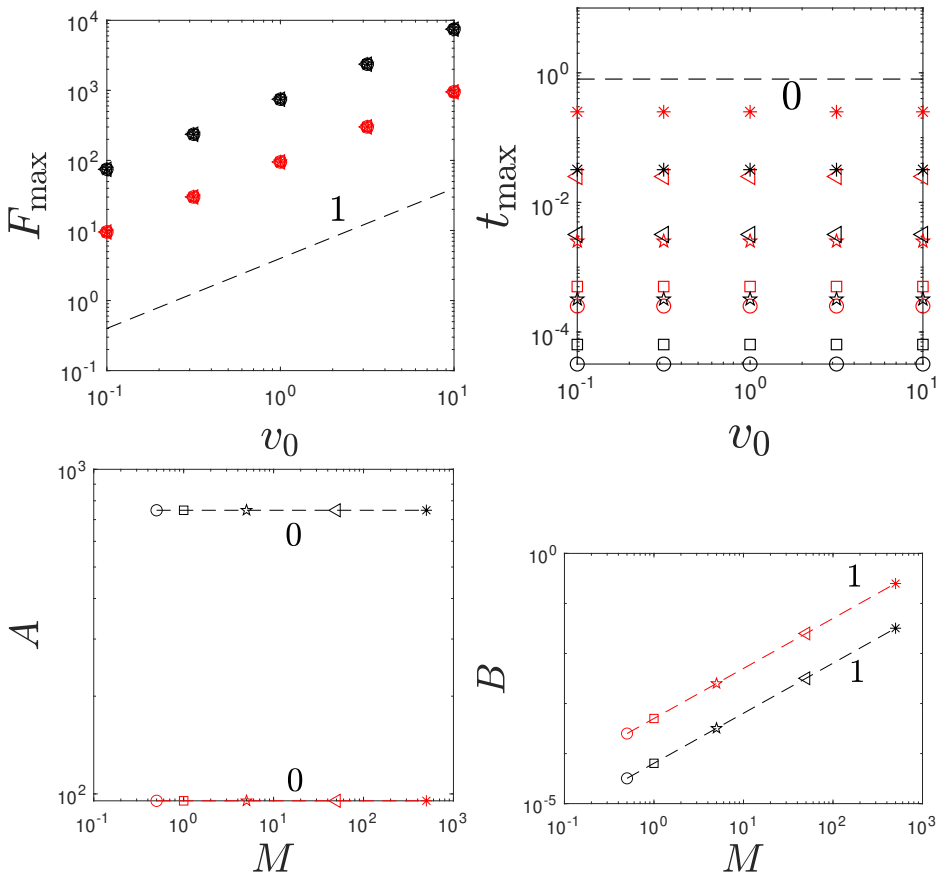

Figure 5.5. Plots for all masses and an α of 0 and a rectangular/columnar added mass profile. Red colors represent the 2D added mass shape, black colors represent the 3D added mass shape, and symbols in order of ascending M are circle, square, pentagram, triangle, asterisk.

5.4 Conclusion

We found that the Waitukaitis added mass model and our simplified model are both captured by the following equations:

$$F_{\max} = A v_0^{1+\alpha}$$
$$A = C M^{\frac{d-1}{d}}$$
$$t_{\max} = B v_0^{-\alpha}$$
$$B = D M^{\frac{1}{d}}$$

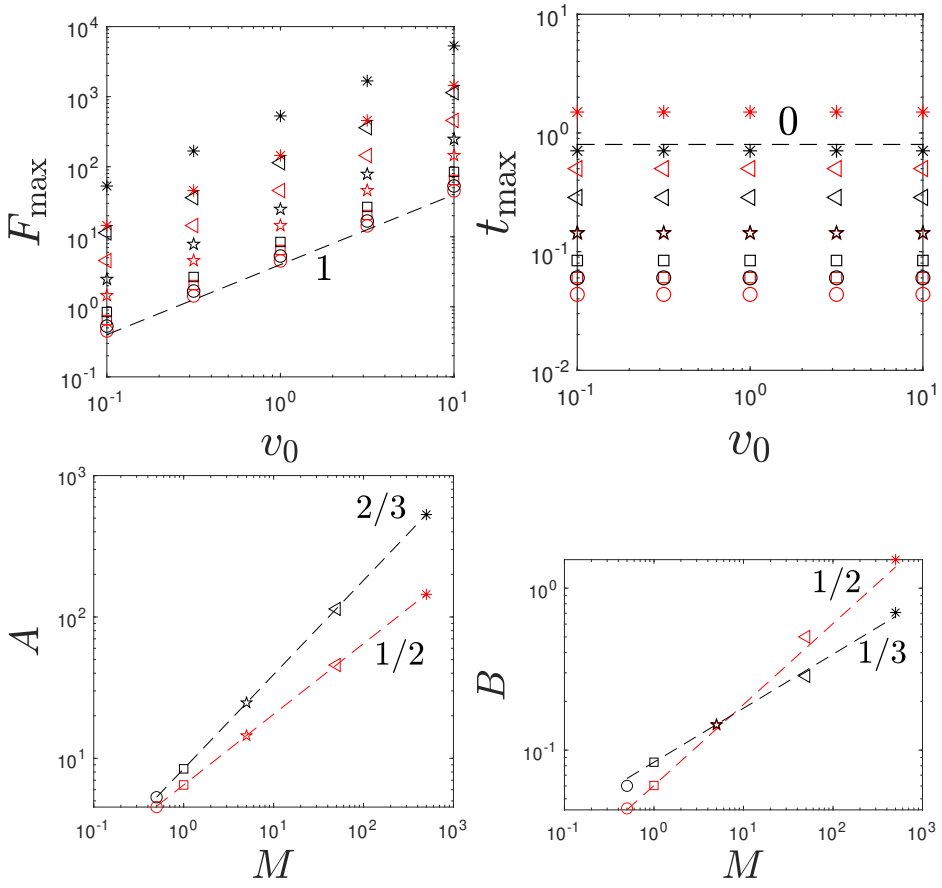

Figure 5.6. Plots for all masses and an α of 0 and a triangular/conic added mass profile. Red colors represent the 2D added mass shape, black colors represent the 3D added mass shape, and symbols in order of ascending M are circle, square, pentagram, triangle, asterisk.

and solved for $F_{\max}$ and $t_{\max}$ to obtain

$$F_{\max} = CM^{1-\frac{1}{d}} v_0^{1+\alpha}$$
$$t_{\max} = DM^{\frac{1}{d}} v_0^{-\alpha}$$

Multiplying $F_{\max}$ by $t_{\max}$ results in the typical change in momentum, which is experienced by the impactor. The result of this multiplication results in $CDMv_0$, which is proportional to the initial momentum of the intruder.

Our results indicate that the generic scaling that can be expressed by $F = Av_0^{1+\alpha}$ and $t = Bv_0^{-\alpha}$

are the predominant factors that determine impactor behavior in an added mass model. We find that both A and B in these equations have a dependence on dimensionality of the added mass. For 2D added mass profiles, $A \propto M^{1/2}$ and $B \propto M^{1/2}$. For 3D added mass profiles, $A \propto M^{2/3}$ and $B \propto M^{1/3}$.

THIS PAGE INTENTIONALLY LEFT BLANK

CHAPTER 6:
Conclusions

This thesis reviewed current literature in the field of dense suspensions, analyzed simulated and experimental data, and attempted to provide a new model for how a velocity front propagates through a suspension. Perhaps most importantly, this thesis found that Darcy flow and Reynolds dilatancy does not explain the forces experienced by an intruder in a saturated granular bed, and that force is proportional to $1/d$ vice $1/d^2$ where d is particle diameter as stated by Jerome et al. [3].

We found that forces experienced by an intruder in a dense suspension consisting of glass microspheres in a density matched SPT solution are similar to those experienced by an intruder in a cornstarch suspension. This is an important result that suggests it is possible to use inorganic materials to create dense suspensions for use in naval applications. We found in proof-of-concept experiments that it is feasible to use the technique of refractive index matching to image particles in a dense suspension, and that it is a valid topic for potential future theses.

Lastly, we showed that the added mass model does not fully capture the dynamics of an impact into a dense suspension and developed a form of power law that can explain the scaling of impact time and force felt on an intruder. We produced a theoretical model that needs to be tested against experimental data, which was collected in the course of a parallel thesis by Marc Brassard to do just that.

THIS PAGE INTENTIONALLY LEFT BLANK

List of References

[1] B. Allen, B. Sokol, S. Mukhopadhyay, R. Maharjan, and E. Brown, "System-spanning dynamically jammed region in response to impact of cornstarch and water suspensions," *Phys. Rev. E*, vol. 97, p. 052603, May 2018. Available: https://link.aps.org/doi/10.1103/PhysRevE.97.052603

[2] S. R. Waitukaitis and H. M. Jaeger, "Impact-activated solidification of dense suspensions via dynamic jamming fronts," *Nature*, vol. 487, no. 7406, p. 205, 2012.

[3] J. J. S. Jerome, N. Vandenberghe, and Y. Forterre, "Unifying impacts in granular matter from quicksand to cornstarch," *Phys. Rev. Lett.*, vol. 117, no. 9, p. 098003, 2016.

[4] P. O. R. L. F.R.S., "Lvii. on the dilatancy of media composed of rigid particles in contact. with experimental illustrations," *The London, Edinburgh, and Dublin Philosophical Magazine and Journal of Science*, vol. 20, no. 127, pp. 469–481, 1885. Available: https://doi.org/10.1080/14786448508627791

[5] H. Darcy, *Les fontaines publiques de dijon ed 1856*. Hachette Livre-Bnf, 2012.

[6] E. Brown and H. M. Jaeger, "Shear thickening in concentrated suspensions: phenomenology, mechanisms and relations to jamming," *Reports on Progress in Physics*, vol. 77, no. 4, p. 046602, Apr 2014. Available: https://doi.org/10.1088%2F0034-4885%2F77%2F4%2F046602

[7] M. Wyart and M. E. Cates, "Discontinuous shear thickening without inertia in dense non-brownian suspensions," *Phys. Rev. Lett.*, vol. 112, p. 098302, Mar 2014. Available: https://link.aps.org/doi/10.1103/PhysRevLett.112.098302

[8] L. Oyarte Gálvez, S. de Beer, D. van der Meer, and A. Pons, "Dramatic effect of fluid chemistry on cornstarch suspensions: Linking particle interactions to macroscopic rheology," *Phys. Rev. E*, vol. 95, p. 030602, Mar 2017. Available: https://link.aps.org/doi/10.1103/PhysRevE.95.030602

[9] S. R. Waitukaitis, L. K. Roth, V. Vitelli, and H. M. Jaeger, "Dynamic jamming fronts," *EPL (Europhysics Letters)*, vol. 102, no. 4, p. 44001, May 2013. Available: https://doi.org/10.1209%2F0295-5075%2F102%2F44001

[10] N. Krizou and A. H. Clark, "Power-law scaling of early-stage forces during granular impact," *Phys. Rev. Lett.*, vol. 124, p. 178002, Apr 2020. Available: https://link.aps.org/doi/10.1103/PhysRevLett.124.178002

[11] S. Mukhopadhyay, B. Allen, and E. Brown, "Testing constitutive relations by running and walking on cornstarch and water suspensions," *Phys. Rev. E*, vol. 97, p. 052604, May 2018. Available: https://link.aps.org/doi/10.1103/PhysRevE.97.052604

[12] I. GeoLiquids, "Heavy liquids safety data sheets," GeoLiquids Inc., Jul 2017. Available: https://geoliquids.com/sds-sheets/

[13] M.-S. Corporation, "Gl0179 data sheet," Mo-Sci Corporation, Mar 2020. Available: https://mo-sci.com/wp-content/uploads/product-docs/glass-microspheres/

[14] M.-S. Corporation, "Gl0191 data sheet," Mo-Sci Corporation, Mar 2020. Available: https://mo-sci.com/wp-content/uploads/product-docs/glass-microspheres/

[15] J. A. Dijksman, N. Brodu, and R. P. Behringer, "Refractive index matched scanning and detection of soft particles," *Review of Scientific Instruments*, vol. 88, no. 5, p. 051807, 2017. Available: https://doi.org/10.1063/1.4983047

[16] J. A. Dijksman, F. Rietz, K. A. Lőrincz, M. van Hecke, and W. Losert, "Invited article: Refractive index matched scanning of dense granular materials," *Review of Scientific Instruments*, vol. 83, no. 1, p. 011301, 2012. Available: https://doi.org/10.1063/1.3674173

[17] A. Fall, F. Bertrand, D. Hautemayou, C. Mezière, P. Moucheront, A. Lemaître, and G. Ovarlez, "Macroscopic discontinuous shear thickening versus local shear jamming in cornstarch," *Phys. Rev. Lett.*, vol. 114, p. 098301, Mar 2015. Available: https://link.aps.org/doi/10.1103/PhysRevLett.114.098301

[18] N. Fernandez, R. Mani, D. Rinaldi, D. Kadau, M. Mosquet, H. Lombois-Burger, J. Cayer-Barrioz, H. J. Herrmann, N. D. Spencer, and L. Isa, "Microscopic mechanism for shear thickening of non-brownian suspensions," *Phys. Rev. Lett.*, vol. 111, p. 108301, Sep 2013. Available: https://link.aps.org/doi/10.1103/PhysRevLett.111.108301

[19] T. T. Truscott, B. P. Epps, and J. Belden, "Water entry of projectiles," *Annual Review of Fluid Mechanics*, vol. 46, no. 1, pp. 355–378, 2014. Available: https://doi.org/10.1146/annurev-fluid-011212-140753

[20] L. R. Gómez, A. M. Turner, M. van Hecke, and V. Vitelli, "Shocks near jamming," *Phys. Rev. Lett.*, vol. 108, p. 058001, Jan 2012. Available: https://link.aps.org/doi/10.1103/PhysRevLett.108.058001

[21] A. H. Clark, A. J. Petersen, L. Kondic, and R. P. Behringer, "Nonlinear force propagation during granular impact," *Phys. Rev. Lett.*, vol. 114, p. 144502, Apr 2015. Available: https://link.aps.org/doi/10.1103/PhysRevLett.114.144502

Initial Distribution List

1. Defense Technical Information Center
   Ft. Belvoir, Virginia

2. Dudley Knox Library
   Naval Postgraduate School
   Monterey, California